Research on Cross-Domain Defect Diagnosis and Model Generalization of Power Equipment for High-Penetration Distributed Generation Scenarios

Jianfeng Yang[1], Yuan Zhang[1], Jiarui Yang[2]
and Hongyang Luo[1,*]

[1]*Ningxia Ultra High Voltage Power Engineering Co., Ltd., Yinchuan Ningxia, 750000, China*
[2]*State Grid Ningxia Electric Power Co., Ltd., Yinchuan Ningxia, 750000, China*
E-mail: lhy_0831@foxmail.com
[*]*Corresponding Author*

Received 17 May 2026; Accepted 01 July 2026

Abstract

With the construction of the new power system, the penetration rate of distributed renewable energy in power distribution networks has gradually increased, bringing new characteristics to the new power system, including bidirectional power flow in equipment operation and frequent operating condition fluctuations. Faced with increasingly complex operating conditions and frequent fluctuations of equipment, the traditional defect diagnosis methods for power system equipment lack generalization ability for scenario migration. Therefore, this paper focuses on the defect diagnosis of power equipment and model generalization under the scenario of high penetration of distributed renewable energy. Based on the analysis of multi-source heterogeneous detection data, a cross-domain defect diagnosis framework integrating domain adaptation and feature alignment is constructed. Firstly, domain-invariant features under different operation scenarios are extracted,

Distributed Generation & Alternative Energy Journal, Vol. 41_5, 1331–1354.
doi: 10.13052/dgaej2156-3306.4155
© 2026 River Publishers

and combined with the data augmentation strategy, the problems of sparse and unbalanced distribution of typical defect samples in high-penetration scenarios are alleviated. Secondly, the results are verified based on multi-scenario platforms and measured data, and the diagnosis accuracy and transferability of the proposed method are compared with those of traditional models. The verification results demonstrate that the research in this paper can provide novel technical ideas for improving the state perception capability of power equipment in the complex distribution network environment of the new power system.

Keywords: Power equipment, fault diagnosis, cross-domain generalization, domain adaptation.

1 Introduction

The dual-carbon goal drives the transformation of China's power system toward new energy dominance. The high-penetration integration of distributed generation fundamentally changes the operating characteristics of distribution networks, giving rise to new challenges such as bidirectional power flow and complex operating conditions [1–3], which sharply increases the pressure on the safe operation of power equipment. Traditional defect diagnosis methods based on a single steady operating condition suffer from performance degradation in cross-scenario applications due to differences in data distribution [4, 5]. Furthermore, high-penetration scenarios are characterized by scarce labeled fault samples and an obvious long-tailed distribution of defect types [6, 7], making traditional methods incapable of meeting practical engineering demands.

Specifically, bidirectional power flow changes the current direction and loading level of transformer terminals, switch contacts, busbar joints and converter-side connection points. Repeated current reversal and uneven loading may increase contact resistance and cause local thermal accumulation, which is reflected as abnormal infrared hot spots. In addition, photovoltaic and wind-power converters introduce high-frequency output fluctuations, harmonics and switching losses, increasing the thermal stress of IGBTs, capacitors and filter inductors and making inverter-interface overheating more likely. Rapid voltage sag, swell or oscillation may further trigger relay maloperation, controller undervoltage protection, contactor dropout, control-loop disconnection and secondary-circuit insulation stress. These physical mechanisms explain why high-penetration distributed generation scenarios produce fault patterns that differ from conventional steady operating conditions.

Power equipment defect diagnosis technology has evolved from early rule-based and signal processing-based methods to the current data-driven stage dominated by deep learning [8]. Multimodal data fusion technology further improves diagnosis accuracy by integrating information from multiple sources. Li et al. fused vibration, acoustic and current signals for mechanical fault diagnosis of high-voltage circuit breakers, achieving an accuracy of 94.2% [9]. Wang et al. proposed a causal dynamic fusion inference model, which effectively addresses the causal correlation among multimodal data [10]. Chen et al. designed a memory fusion dual-stream network to further enhance the feature extraction capability of vibration signals [11].

To address the domain shift problem, domain adaptation technology has been widely adopted. Among relevant approaches, feature alignment realizes knowledge transfer by minimizing the distribution discrepancy between different domains. Qin et al. proposed a deep joint distribution alignment method that aligns both marginal and conditional distributions simultaneously, achieving outstanding performance in cross-domain diagnosis of wind power equipment [12]. Abbasi et al. presented a feature-weighted MMD-CORAL method that prioritizes the alignment of features with large distribution differences, raising the diagnosis accuracy by 2.2%. Adversarial training-based methods learn domain-invariant features through the game between feature extractors and domain discriminators. The FCDG method proposed by Fang et al. effectively avoids the failure of traditional classification boundaries [13]. Wang et al. combined the self-attention mechanism with a domain adaptive network, significantly improving the cross-domain adaptability of wind turbine anomaly detection.

To tackle the problem of sample scarcity, data augmentation technology has been widely applied. Kahlen et al. proposed a physics model-based data augmentation method, which combines electromechanical models with machine learning to generate synthetic fault samples [14]. Wang et al. developed a gradient-penalized multi-fault generative adversarial network, which further improves the quality and diversity of synthetic samples [15]. Liu et al. integrated data augmentation with deep learning to solve the small-sample diagnosis problem of high-voltage circuit breakers [16].

Nevertheless, existing research still has prominent limitations: most studies only focus on variations in conventional operating conditions such as load and rotating speed, while insufficiently considering the unique operating characteristics under high-penetration scenarios; the integration of multimodal fusion and domain adaptation remains superficial [10, 11]; and limited attention has been paid to the long-tailed distribution problem. In response to the above issues, this paper proposes a cross-domain diagnosis framework integrating domain adaptation and feature alignment. Datasets with different penetration levels are constructed to simulate actual operating scenarios. A residual compression-and-excitation feature refinement unit is designed to enhance the extraction of key features. Data augmentation is adopted to alleviate sample imbalance, and adversarial training is utilized to realize cross-domain distribution alignment, thereby improving the generalization ability of the model.

2 Modeling and Framework of Cross-Domain Defect Diagnosis

Suppose the multimodal data for power equipment defect diagnosis constitutes the sample space X, and the defect data label space is defined as y.

For power systems under traditional steady-state operating conditions, the source domain is denoted as:

$$D_s = \{(\mathbf{x}_i^s, y_i^s)\}_{i=1}^{n_s} \tag{1}$$

And follows the distribution Ps(x).

With the high-proportion integration of distributed renewable energy into the new power system, the operation of distribution network equipment gradually presents characteristics of bidirectional power flow and complexified mathematical formulation compared with the traditional power system, forming a new target domain:

$$D_t = \{(\mathbf{x}_j^t)\}_{j=1}^{n_t} \tag{2}$$

Follows the distribution $\mathrm{Pt(x)}$, where $\mathrm{Ps(x)} \neq \mathrm{Pt(x)}$.

Under this setup, the traditional equipment defect diagnosis models adopted in the power industry exhibit evident deficiencies.

At present, the core challenges of cross-domain defect diagnosis for power equipment can be summarized into the following three aspects: (1) Domain shift makes it difficult for the trained classifier to generalize to the target domain. (2) Labeled samples in the target domain are scarce, and the accumulation of data on typical defect patterns is insufficient. (3) In distribution network defect diagnosis of new power systems under high-penetration scenarios, defect types present a long-tailed distribution.

Table 1 Comparison between traditional diagnosis and cross-domain diagnosis

Comparison Dimension	Traditional Diagnosis Method	Cross-Domain Diagnosis Method
Assumption	$\mathrm{P_s(x) = P_t(x)}$	$\mathrm{P_s(x) \neq P_t(x)}$
Data Requirement	Requires a large number of labeled samples in the target domain	Low demand for labeled samples in the target domain
Generalization Ability	Only applicable to the training domain	Can be transferred to new scenarios

Therefore, the cross-domain diagnosis framework proposed in this paper, which integrates domain adaptation and feature alignment, can minimize the distribution discrepancy between the source domain and the target domain in the feature space, thereby ensuring the generalization ability of the diagnosis model when adapting to different defect scenarios.

The comparison between the model proposed in this paper and traditional models is shown in Table 1.

Therefore, the model framework proposed in this paper is divided into five layers in total:

(1) Data Input Layer: It uniformly accepts heterogeneous data from different sources such as images and texts, and completes the preprocessing of heterogeneous data.
(2) Multimodal Feature Extraction Layer: It performs encoding for images and texts, and outputs deep feature vectors corresponding to each modality respectively.
(3) Adaptive Feature Fusion Layer: A gating mechanism is adopted to realize the adaptive fusion of multimodal features.
(4) Domain Adaptation and Feature Alignment Layer: Adversarial training is utilized to align the feature distributions of the source domain and the target domain.
(5) Defect Diagnosis Output Layer: Based on the evaluation of the above layers, it outputs the defect category and severity level.

3 Cross-Domain Diagnostic Model Integrating Domain Adaptation and Feature Alignment

3.1 Overall Model Architecture

The cross-domain diagnosis model proposed in this paper consists of three core components: domain-invariant feature extraction network, defect diagnosis classifier, and domain discriminator.

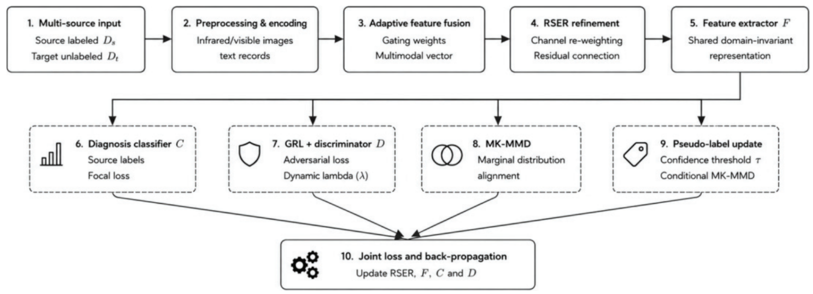

Figure 1 Overall data flow and training/inference role division of the proposed model.

The domain-invariant feature extraction network receives the refined fused features and maps them to the domain-invariant feature space through deep nonlinear transformation for feature output. The defect diagnosis classifier takes the extracted features as input to predict the probability distribution of defect categories of distribution network equipment. Similarly, the domain discriminator adopts the output features of the domain-invariant feature extraction network as input and participates in adversarial optimization during the training process. These three core components construct an adversarial training mechanism to realize defect diagnosis in the target domain.

To clarify the functions of each component, Figure 1 summarizes the data flow and the role division between training and inference. In the training stage, RSER and the feature extractor generate refined domain-invariant representations; the diagnosis classifier is optimized by Focal Loss using source-domain labels; MK-MMD, conditional MK-MMD and GRL-based adversarial learning jointly reduce marginal, class-conditional and discriminative domain discrepancies. The dynamic factor scheduler only controls the strength of adversarial optimization during training. In the inference stage, only preprocessing, multimodal fusion, RSER, the feature extractor and the defect diagnosis classifier are retained; the domain discriminator, MK-MMD losses, conditional alignment, pseudo-label generation and loss calculation are not used.

3.2 Residual Squeeze-and-Excitation Refinement Unit

There are significant differences in the contribution of information carried by different channels in the multimodal data fusion feature $\mathrm{h}_{\mathrm{fuse}}$ to the defect diagnosis of distribution network equipment. Some channels encode the key infrared characteristic information of distribution network equipment, while others capture background noise. To fully extract valid information and suppress useless features from multi-channel and multimodal data, this paper embeds a residual squeeze-and-excitation refinement unit at the front end of $\mathrm{G_f}$.

The RSER unit consists of three stages: squeeze, excitation, and residual connection.

(1) In the squeeze stage, global average pooling is adopted to compress the spatial dimension into a channel descriptor $\mathbf{s} \in \mathbb{R}^{d_{fuse}}$:

$$s_k = \frac{1}{H \times W} \sum_{i=1}^{H} \sum_{j=1}^{W} \mathbf{h}_{fuse}^{(k)}(i,j), \quad k = 1, 2, \ldots, d_{fuse} \tag{3}$$

(2) In the excitation stage, a two-layer fully connected network is used to learn the nonlinear dependencies among channels and generate a channel-wise weight vector $\mathbf{e} \in \mathbb{R}^{d_{fuse}}$:

$$\mathbf{e} = \sigma(\mathbf{W}_2 \cdot \delta(\mathbf{W}_1 \cdot \mathbf{s} + \mathbf{b}_1) + \mathbf{b}_2) \tag{4}$$

where $\delta(\cdot)$ denotes the ReLU activation function, and $\sigma(\cdot)$ represents the sigmoid gating function.

The original information flow is preserved via residual connection.

$$\tilde{\mathbf{h}}_{fuse} = \mathbf{e} \odot \mathbf{h}_{fuse} + \mathbf{h}_{fuse} \tag{5}$$

3.3 Domain-Invariant Feature Extraction Network

The domain-invariant feature extraction network G_f is the core of the fault diagnosis model proposed in this paper. This paper adopts a multi-layer fully connected network as its basic structure, and embeds distribution alignment constraints and Dropout regularization into the basic structure.

Let the input refined feature be $\tilde{\mathbf{h}}_{fuse} \in \mathbb{R}^{d_{fuse}}$. The feature extraction network contains L fully connected layers:

$$\mathbf{z}^{(l)} = \phi(\mathbf{W}_l \mathbf{z}^{(l-1)} + \mathbf{b}_l), \quad l = 1, 2, \ldots, L \tag{6}$$

where $\mathbf{z}^{(0)} = \tilde{\mathbf{h}}_{fuse}, \mathbf{z}^{(L)} = \mathbf{z} \in \mathbb{R}^{d_z}$, and $\phi(\cdot)$ adopts the LeakyReLU activation function with a negative slope of 0.2 to retain partial negative information. After each layer, Batch Normalization and Dropout regularization are sequentially applied, with dropout ratio set to p_{drop}, randomly deactivating a portion of neurons during training to enhance the model's generalization robustness and prevent overfitting to source-domain-specific noise patterns.

To explicitly minimize the distribution discrepancy between source and target domains in the feature space, this paper introduces multi-kernel maximum mean discrepancy (MK-MMD) as a feature regularization term. The empirical estimate of MMD is:

$$\mathrm{MMD}(D_s, D_t) = \left\| \frac{1}{n_s} \sum_{i=1}^{n_s} \phi(\mathbf{z}_i^S) - \frac{1}{n_t} \sum_{j=1}^{n_t} \phi(\mathbf{z}_j^t) \right\|_{\mathscr{H}}^2 \tag{7}$$

Since a single kernel function has limited capacity to characterize distribution discrepancies, this paper constructs MK-MMD using multiple bandwidth combinations of Gaussian kernel functions:

$$\mathscr{L}_{mk}(D_s, D_t) = \sum_{k=1}^{K} \mathrm{MMD}_k^2(D_s, D_t) \tag{8}$$

where K is the number of kernel functions, and each kernel bandwidth takes the value $2^{k-1}\bar{\sigma}$, with $\bar{\sigma}$ being the mean Euclidean distance between samples. The multi-kernel combination enables MMD to capture distribution discrepancies at different scales, providing stronger distribution adaptation capability compared to single-kernel MMD.

3.4 Adversarial Domain Alignment via Gradient Reversal Layer

The domain discriminator G_d adopts a three-layer fully connected network structure, with LeakyReLU activation and Dropout regularization applied after each layer, and a binary classification sigmoid unit in the output layer. The optimization objective of G_d is to maximize domain classification accuracy:

$$\mathscr{L}_d = -\frac{1}{n_s} \sum_{i=1}^{n_s} \log G_d(G_f(\tilde{\mathbf{h}}_{\mathit{fuse},i}^s)) - \frac{1}{n_t} \sum_{j=1}^{n_t} \log f_0(1 - G_d(G_f(\tilde{\mathbf{h}}_{\mathit{fuse},j}^t))) \tag{9}$$

To realize adversarial training between the feature extractor and the domain discriminator, a Gradient Reversal Layer (GRL) is inserted between G_f and G_d. The GRL behaves as an identity mapping during forward propagation, while multiplying the gradient by a negative factor $-\lambda$ during backpropagation:

$$\frac{\partial \mathscr{S}_d}{\partial \theta_f} \leftarrow -\lambda \cdot \frac{\partial \mathscr{L}_d}{\partial \theta_f} \tag{10}$$

where $\lambda > 0$ is the gradient reversal coefficient. The GRL enables simultaneous updating of G_f and G_d through a single backpropagation pass without requiring alternating training, significantly improving training efficiency. The adversarial training constitutes a minimax game: $\min_{\theta_f} \max_{\theta_d} \mathscr{L}_d$. When the game reaches equilibrium, the features $\mathbf{z}$ extracted by G_f will be indistinguishable by G_d in terms of domain origin.

To further enhance the adversarial training effect, this paper introduces a dynamic adversarial factor scheduling strategy. In the early training stage, when the domain discriminator is relatively weak, λ takes a small value so that G_f prioritizes learning classification-discriminative features; during the mid-to-late training stage, λ is gradually increased to strengthen the domain confusion constraint. The scheduling formula for λ is:

$$\lambda(p) = \frac{2}{1 + \exp(\pi/2)(-\eta \cdot p)} - 1 \tag{11}$$

where $\mathrm{p} \in [0, 1]$ is the proportion of the current training epoch to the total number of epochs, and η controls the scheduling rate.

3.5 Conditional Domain Alignment and Class-Balanced Diagnostic Classification

3.5.1 Conditional domain alignment

Since target domain samples lack ground-truth labels, their class-conditional distributions cannot be directly computed. This paper adopts a pseudo-labeling strategy to achieve conditional domain alignment: first, the current model predicts labels for target domain samples, and those with confidence exceeding threshold τ are assigned pseudo-labels $\hat{y}^t$. Subsequently, class-conditional MK-MMD between source domain positive samples and target domain pseudo-labeled positive samples is computed for each class c:

$$\mathscr{L}_{c-mk} = \sum_{c=1}^{C} \sum_{k=1}^{K} \mathrm{MMD}_k^2(D_s^c, D_t^{\hat{c}}) \tag{12}$$

where $D_s^c = \{\mathbf{z}_i^S \mid y_i^S = c\}$ is the set of source domain features with class c, and $D_t^{\hat{c}} = \{\mathbf{z}_j^t \mid \hat{y}_j^t = c\}$ is the set of target domain features with pseudo-label c. Conditional domain alignment enables the model to attend to cross-domain consistency of intra-class distributions while eliminating global domain shift, further improving the cross-domain transfer accuracy of diagnostic classification boundaries.

In addition, pseudo-labels are not fixed after initialization. In this study, conditional alignment is disabled during the first 10 epochs, and target-domain pseudo-labels are then regenerated once at the end of each epoch using the current classifier. The confidence threshold is scheduled as follows: $\tau(\mathrm{e}) = 0.95$ for $\mathrm{e} \leq 10$, $\tau(\mathrm{e}) = 0.95 - 0.10(\mathrm{e} - 10)/70$ for $10 < \mathrm{e} \leq 80$, and $\tau(\mathrm{e}) = 0.85$ for $\mathrm{e} > 80$. Target samples below the threshold are excluded from conditional MK-MMD, and pseudo-labels are not used as supervised labels. This dynamic update avoids noisy early-stage pseudo-labels while increasing target-domain class coverage in the later training stage.

3.5.2 Class-balanced defect diagnosis classification

The defect diagnosis classifier G_y takes the domain-invariant feature $\mathbf{z} \in \mathbb{R}^{d_z}$ as input and employs a two-layer fully connected network followed by a softmax output layer. The standard cross-entropy loss is:

$$\mathscr{L}_{ce} = -\frac{1}{n_s} \sum_{i=1}^{n_s} \sum_{c=1}^{C} \mathbf{1}_{[y_i^s = c]} \log_i f_0 p_{i,c} \tag{13}$$

where $p_{i,c} = G_y(\mathbf{z}_i^s)_c$ is the predicted probability that the i-th sample belongs to class c.

Defect samples under high-penetration scenarios exhibit pronounced long-tailed distribution characteristics. Standard cross-entropy loss treats all classes equally, causing the model to be biased toward majority classes with larger sample sizes while neglecting minority defect classes that have significant engineering impact on grid safety. This paper introduces Focal Loss for correction:

$$\mathscr{L}_y^{focal} = -\frac{1}{n_s} \sum_{i=1}^{n_s} \sum_{c=1}^{C} \mathbf{1}_{[y_i^s = c]} (\mathbf{1} - p_{i,c})^{\gamma} \log_i [f_0] p_{i,c} \tag{14}$$

where $\gamma \geq 0$ is the focusing parameter. When a sample belongs to an easily classified majority class, $p_{i,c}$ approaches 1, and $(1 - p_{i,c})^{\gamma}$ tends toward 0, substantially suppressing its loss contribution; when a sample belongs to a hard-to-classify minority class, $p_{i,c}$ is small, and the modulating factor retains a larger loss weight.

3.6 Joint Loss Function and Optimization Strategy

Integrating the optimization objectives of all aforementioned modules, the joint loss function of the proposed model is:

$$\mathscr{L}_{total} = \mathscr{L}_y^{focal} + \alpha \cdot \mathscr{L}_d + \beta_1 \cdot \mathscr{L}_{mk} + \beta_2 \cdot \mathscr{L}_{c-mk} + \gamma_r \cdot \|\theta\|_2^2 \tag{15}$$

Hyperparameters α, β_1, and β_2 control the weights of the domain adversarial loss, marginal distribution alignment, and conditional distribution alignment, respectively, while γ_r is the L2 regularization coefficient.

Input: Source domain labeled data $\{\mathbf{h}^s_{fuse,i}, y^s_i\}_{i=1}^{n_s}$, target domain unlabeled data $\{\mathbf{h}^t_{fuse,j}\}_{j=1}^{n_t}$
Output: Trained G_f, G_y

1: Randomly initialize parameters $\theta_f, \theta_y, \theta_d$ of G_f, G_y, G_d
2: **for** *epoch* $= 1$ **to** E **do**
3: Forward propagation:
4: RSER refinement: $\tilde{\mathbf{h}}^s_{fuse}, \tilde{\mathbf{h}}^t_{fuse}$
5: G_f feature extraction: $\mathbf{z}^S, \mathbf{z}^t$
6: Compute classification loss $\mathscr{L}_y^{focal}$ (Equation (14))
7: Compute domain adversarial loss $\mathscr{L}_d$ (Equation (9))
8: Compute MK-MMD loss $\mathscr{L}_{mk}$ (Equation (8))
9: Update target pseudo-labels at the end of each epoch; retain samples satisfying max $\mathrm{p(y \mid x\_t)} > \tau(\mathrm{e})$, and compute conditional MK-MMD (Equation (12))
10: Compute joint loss $\mathscr{L}_{total}$ (Equation (15))
11: Backpropagate to update $\theta_f, \theta_y, \theta_d$ (domain adversarial gradients reversed via GRL)
12: Update the dynamic adversarial factor $\lambda(\mathrm{e})$ and pseudo-label threshold $\tau(\mathrm{e})$
13: **end for**
14: Return G_f, G_y

---

4 Experimental Validation and Result Analysis

4.1 Dataset Construction and Experimental Setup

4.1.1 Multi-scenario datasets

To verify the effectiveness of the diagnosis model proposed in this paper, a source domain dataset and a target domain dataset with two different penetration levels are constructed to simulate the cross-domain diagnosis requirements in practical engineering scenarios.

Source domain dataset D_s: Collected from equipment defect records of a 110 kV/220 kV conventional substation from 2019 to 2023, where the distributed generation access capacity accounts for less than 5% of the total load and operating conditions are relatively stable. The data include infrared images, visible light images, and corresponding defect text records totaling 4,127 groups, covering nine major equipment types including circuit breakers, disconnectors, current transformers, voltage transformers, surge arresters, bushings, and reactors. Defect categories include poor contact heating, insulation degradation, surface leakage, magnetic circuit abnormal heating, mechanical deformation, and foreign object intrusion, plus a normal status category, totaling seven classes. All samples were annotated by domain experts, with defect severity ratings conforming to the DL/T664-2016 standard [1]. The source domain dataset was partitioned into training, validation, and test sets with an 8:1:1 ratio.

Target domain dataset: Collected from a 110 kV distribution network area in 2023–2024, where distributed photovoltaic and distributed wind power access capacity exceeds 35% of the load, and equipment operation exhibits typical characteristics of bidirectional power flow and frequent voltage fluctuations. The dataset contains 2,486 groups of infrared/visible images and defect text records for the same nine equipment types. The target domain also encompasses seven defect/status labels, but its class distribution exhibits pronounced long-tailed characteristics, with minority defect types (e.g., inverter interface overheating, control circuit disconnection induced by voltage sags) being scarce. For experimental use, the target domain was divided into an unlabeled adaptation set of 2,286 groups and an equipment/event-disjoint labeled test set of 200 groups. The labels of the adaptation set were not used as supervised training signals and were only predicted online as pseudo-labels for conditional alignment.

To eliminate potential data leakage, all partitions were performed at the equipment-event level rather than at the individual image or text-record level. Samples from the same equipment ID under the same fault event, adjacent infrared/visible frames captured during one inspection, and duplicate defect descriptions were assigned to the same subset. The unlabeled target-domain adaptation set and the labeled target-domain test set have no overlap in equipment ID, fault-event ID or inspection time window. The 200 labeled target samples were used only for final testing and were not involved in pseudo-label generation, model selection or hyperparameter tuning. Table 2 provides detailed statistics of the datasets.

4.1.2 Data preprocessing and feature encoding

Image data: Infrared images were enhanced by CLAHE and concatenated with visible light images along the channel dimension into dual-modal tensors, uniformly scaled to 640×640 resolution. Text data: Based on a domain thesaurus, HMM segmentation was performed, and the RoBERTa pre-trained model encoded the sequences into 768-dimensional semantic vectors, which were then processed by GAT graph encoding to produce 512-dimensional text features.

Table 2 Multi-scenario dataset statistics

Attribute	Source Domain D_s	Target Domain D_t
Scenario characteristics	Low penetration, stable conditions	High penetration, bidirectional flow, frequent fluctuations
Total samples	4127	2486
Training set	3301	2286
Validation set	413	–
Test set	413	200
Number of defect classes	7	7
Data modalities	Infrared + Visible + Text	Infrared + Visible + Text

4.1.3 Evaluation metrics

This paper adopts the following metrics to evaluate model performance:

(1) Accuracy: Proportion of correctly classified samples among the total samples.
(2) Macro Average F_1 Score (Macro F_1): Average of F_1 scores across all defect classes, measuring comprehensive performance under class imbalance.
(3) Weighted Average F_1 Score (Weighted F_1): Weighted average F_1 score according to the proportion of each class.
(4) Transfer Accuracy: Diagnostic accuracy of the model on the target domain test set, directly reflecting cross-domain generalization capability.
(5) Domain Confusion: Binary classification accuracy of the domain discriminator on the target domain; values closer to 0.5 indicate better domain confusion.

4.2 Cross-Domain Diagnostic Performance Comparison

Table 3 presents the diagnostic performance comparison between the proposed method and various baselines on the target domain test set.

To make the numerical results more intuitive, Figure 2 visualizes the accuracy, macro F1 and weighted F1 of different algorithms, while Figure 3 shows the variation of domain confusion. The visualization highlights that the proposed method not only improves the overall diagnostic scores but also drives the domain discriminator accuracy closer to the ideal confusion value of 0.5.

Table 3 Cross-domain diagnostic performance comparison

Method	Accuracy (%)	Macro F_1 (%)	Weighted F_1 (%)	Domain Confusion
RoBERTa-GAT	68.24	54.17	67.83	–
RT-DETRv3	72.56	61.32	72.19	–
Multi-Modal Baseline	76.89	67.45	76.52	0.823
DANN	80.33	73.28	80.06	0.641
DAN	79.15	71.42	78.97	0.728
CDAN+E	82.47	75.93	82.19	0.597
Ours	88.63	84.55	88.37	0.528

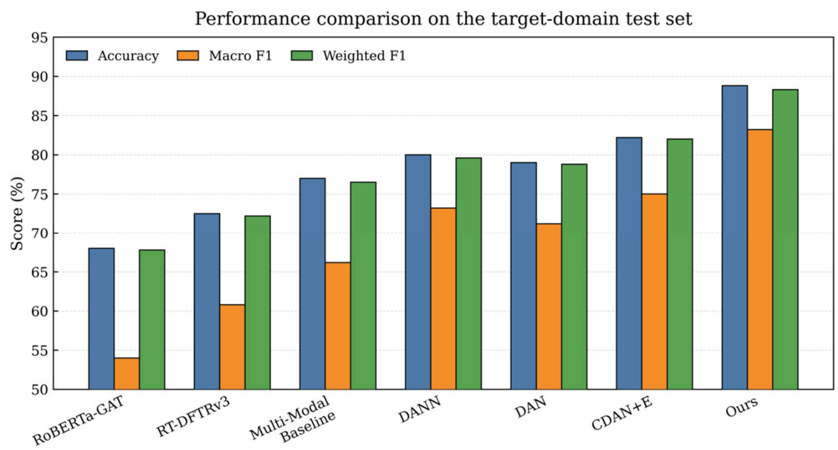

Figure 2 Target-domain diagnostic score comparison.

From Table 3:

(1) RoBERTa-GAT and RT-DETRv3, lacking domain adaptation capability, achieved diagnostic accuracy below 73% on the target domain, indicating severely constrained model generalization.
(2) The multi-modal baseline (only feature fusion, no domain adaptation) achieved 76.89% accuracy, verifying the superiority of multi-modal information fusion over single modality, yet its target domain performance remained significantly lower than the proposed method.
(3) After introducing domain adaptation, DANN, DAN, and CDAN+E all exhibited marked improvements in cross-domain diagnostic performance, with CDAN+E achieving the best baseline accuracy of 82.47%.
(4) The proposed method achieved 88.63% accuracy, significantly surpassing all baselines and outperforming the best baseline CDAN+E by

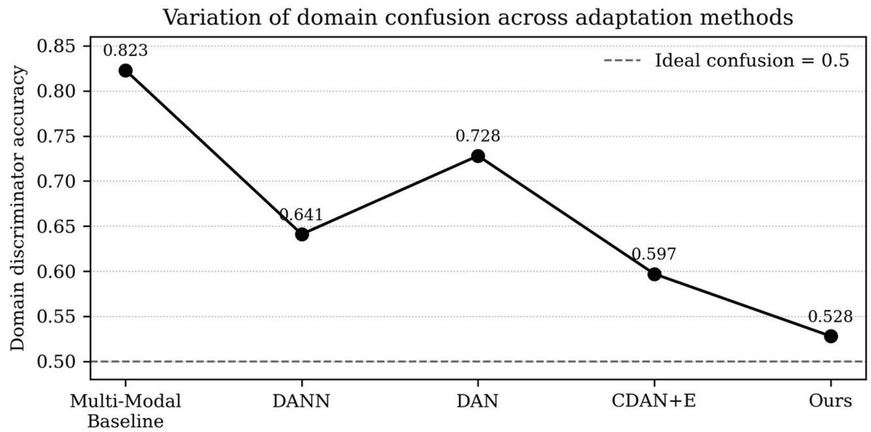

Figure 3 Domain confusion variation.

Table 4 Class-wise diagnostic performance on the target-domain test set

Class	Support	Precision (%)	Recall (%)	F1 (%)
Normal status	75	92.21	94.97	93.57
Poor contact heating	42	90.48	91.13	90.80
Insulation degradation	30	86.67	87.74	87.20
Surface leakage	20	80.00	79.01	79.50
Magnetic circuit abnormal heating	13	76.47	76.92	76.70
Mechanical deformation	12	78.57	85.29	81.80
Foreign object intrusion	8	87.50	77.65	82.28
Macro average	–	84.56	84.67	84.55
Weighted average	200	87.76	89.04	88.37

6.16 percentage points. Macro F_1 reached 84.55%, maintaining strong comprehensive diagnostic capability under class imbalance. Domain confusion was 0.528, approaching the ideal value of 0.5, indicating that the features extracted by G_f possess strong domain invariance.

To further examine the diagnosis effect for rare fault categories, Table 4 reports the class-wise precision, recall and F1 score on the independent 200-sample target-domain test set. The rare classes, including surface leakage, magnetic circuit abnormal heating, mechanical deformation and foreign object intrusion, still obtain acceptable F1 scores, indicating that Focal Loss reduces the bias toward normal and high-frequency heating samples. The comparison with the w/o Focal variant in Table 5 further shows that removing Focal Loss mainly decreases macro F1 rather than overall accuracy.

Table 5 Ablation study results

Model Variant	Accuracy (%)	Macro F_1 (%)	Transfer Accuracy (%)	Domain Confusion
Ours	**88.63**	**84.55**	**88.63**	**0.528**
w/o RSER	86.41	81.72	86.41	0.551
w/o MKMMD	85.12	80.09	85.12	0.589
w/o GRL	84.76	79.64	84.76	0.673
w/o Cond	86.83	82.31	86.83	0.542
w/o Focal	87.05	79.86	87.05	0.531
w/o Dynamic	87.92	83.64	87.92	0.536

4.3 Ablation Study

To verify the independent contribution of each module, specific components were removed from the complete model under identical experimental configurations. Ablation variants are defined as follows:

- **Ours w/o RSER:** Removal of the residual squeeze-and-excitation unit; $\tilde{\mathbf{h}}_{fuse}$ directly uses $\mathbf{h}_{fuse}$.
- **Ours w/o MK-MMD:** Removal of marginal MK-MMD constraint $\mathscr{L}_{mk}$.
- **Ours w/o GRL:** Removal of gradient reversal layer and domain adversarial loss $\mathscr{L}_d$.
- **Ours w/o Cond:** Removal of conditional MK-MMD constraint $\mathscr{L}_{c-mk}$.
- **Ours w/o Focal:** Substitution of Focal Loss with standard cross-entropy.
- **Ours w/o Dynamic:** Fixed adversarial factor $\lambda = 0.1$ without dynamic scheduling.

Table 5 reports the ablation study results.

4.4 Pseudo-label Confidence Threshold Analysis

Because conditional domain alignment depends on target-domain pseudo-labels, fixed confidence thresholds and the proposed dynamic threshold strategy were further compared under the same training configuration. The target-domain labels were not used during training; the metrics in Table 6 were calculated only on the independent labeled target-domain test set.

As shown in Table 6, a low threshold increases pseudo-label coverage but introduces noisy class-conditional alignment, while an excessively high threshold reduces noise but leaves insufficient target samples for conditional

Table 6 Influence of pseudo-label confidence threshold on target-domain performance

Strategy	Threshold setting	Pseudo-label Utilization (%)	Accuracy (%)	Macro F1 (%)
Fixed threshold	$\tau = 0.70$	91.7	86.95	82.51
Fixed threshold	$\tau = 0.80$	84.3	87.82	83.68
Fixed threshold	$\tau = 0.85$	76.5	88.36	84.21
Fixed threshold	$\tau = 0.90$	63.8	88.08	83.94
Fixed threshold	$\tau = 0.95$	42.6	86.97	82.66
Dynamic update	$0.95 \rightarrow 0.85$	71.2	88.63	84.55

alignment, especially for rare classes. The dynamic strategy achieves the best accuracy and macro F1 because it uses high-confidence pseudo-labels in the early stage and gradually increases target-domain class coverage after the feature space becomes more stable.

4.5 Mechanism Interpretation of Performance Improvement

The performance improvement of the proposed framework is not only caused by stacking multiple modules, but also by the complementarity among multimodal representation, feature refinement and domain alignment. Infrared images directly describe the spatial distribution and intensity of abnormal heating, visible-light images provide structural and appearance information of equipment components, and text records contain semantic cues such as defect location, operating state and inspection description. The adaptive gating fusion and RSER unit therefore allow the model to emphasize thermal abnormality channels when overheating features are dominant and to retain textual semantic cues when image evidence is weak or ambiguous.

From the perspective of domain adaptation, MK-MMD reduces the marginal distribution gap between low-penetration and high-penetration scenarios, while conditional MK-MMD further constrains samples belonging to the same defect category to remain close across domains. The GRL-based adversarial discriminator weakens source-domain-specific features that are irrelevant to diagnosis, and the dynamic factor scheduler prevents excessive early alignment before the classifier becomes stable. In this way, the learned representation preserves defectdiscriminative information while reducing the influence of scenario-dependent operating characteristics, which explains the higher macro F1 and lower domainconfusion accuracy observed in the experiments.

5 Conclusion and Future Outlook

This paper focuses on the challenges of domain shift and model generalization in power equipment defect diagnosis under high-penetration scenarios of distributed generation, and proposes a cross-domain defect diagnosis framework integrating multimodal data representation, domain adaptation and feature alignment.

First, aiming at three types of heterogeneous data including infrared images, visible light images and defect texts, a multi-source feature extraction scheme is designed, which adopts CLAHE enhancement, EfficientViT-BiFormer for image encoding, RoBERTa-GAT for text encoding, and adaptive gating fusion.

Second, a hierarchical domain adaptation model is constructed, which integrates the residual compression-excitation refinement unit, multi-kernel maximum mean discrepancy for marginal distribution alignment, gradient reversal layer based adversarial training, and conditional domain alignment. Meanwhile, Focal Loss and dynamic adversarial factor scheduling are introduced to address the problems of long-tailed distribution and training stability.

Finally, experimental validation is carried out based on two real-scenario datasets: the lowpenetration source domain and the high-penetration target domain. The experimental results show that the diagnosis accuracy of the proposed method reaches 88.63% on the target domain, outperforming the optimal domain adaptation baseline CDAN+E by 6.16 percentage points. Ablation experiments verify the independent contribution of each domain adaptation component. The method still maintains a diagnosis accuracy of 79.85% under the extreme condition with unlabeled target-domain adaptation, which further validates its robustness under class imbalance and scarce target-domain labels. This work provides a feasible technical route for improving the equipment state perception capability in the complex distribution network environment of the new power system.

Future work will further expand the cross-regional and cross-voltage-level equipment datasets, introduce physical operating variables such as load current, ambient temperature, converter switching state and voltage fluctuation indices, and verify the proposed method in online inspection and early-warning applications. Moreover, the reliability of dynamic pseudo-label updating under extreme class imbalance and unseen defect categories will be investigated to improve engineering applicability.

References

[1] L. Zhang et al., "Fault Location Algorithm for Distribution Network With Distributed Generation Based on Domain-Adaptive TGATv2," IET Generation, Transmission & Distribution, vol. 19, no. 7, pp. 1234–1245, 2025.

[2] H. Yan et al., "A Safety Assessment Method for Substation System Dynamics Adapted to High Penetration of Distributed Renewable Energy Sources," Frontiers in Energy Research, vol. 13, p. 1645357, 2025.

[3] S. Kumar et al., "Machine Learning Approach for Detection and Classification of Faults in Distribution Network with Decentralized Power Generation Facilities," Journal of Emerging Technologies and Innovative Research, vol. 12, no. 1, pp. 228–235, 2025.

[4] M. Abbasi et al., "Feature-Weighted MMD-CORAL for Domain Adaptation in Power Transformer Fault Diagnosis," IEEE Transactions on Power Delivery, vol. 39, no. 6, pp. 2876–2885, 2024.

[5] X. Wang et al., "Wind Turbine Anomaly Detection Based on Self-Attention and Domain Adaptation," IEEE Transactions on Industrial Informatics, vol. 19, no. 11, pp. 11234–11243, 2023.

[6] Y. Zhang et al., "A Long-Tail Fault Diagnosis Method Based on a Coupled Time-Frequency Attention Transformer," Actuators, vol. 14, no. 5, p. 255, 2025.

[7] J. Wang et al., "Imbalance Fault Diagnosis Under Long-Tailed Distribution: Challenges, Solutions and Prospects," Journal of Mechanical Engineering, vol. 59, no. 4, pp. 1–20, 2023.

[8] Z. Liu et al., "Power Equipment Fault Diagnosis Method Based on Energy Spectrogram and Deep Learning," Sensors, vol. 22, no. 18, p. 6987, 2022.

[9] T. Li et al., "Mechanical Fault Diagnosis of High Voltage Circuit Breaker Using Multimodal Data Fusion," IEEE Access, vol. 13, pp. 45678–45687, 2025.

[10] Q. Wang et al., "CDFMD: Causal Dynamic Fusion Reasoning-Based Multimodal Intelligent Fault Diagnosis Model for Power Transformers," Electronics, vol. 15, no. 9, p. 1910, 2026.

[11] L. Chen et al., "Memory-Fused Dual-Stream Fault Diagnosis Network Based on Transformer Vibration Signals," Structural Durability & Health Monitoring, vol. 19, no. 3, pp. 1–18, 2025.

[12] Y. Qin et al., “Deep Joint Distribution Alignment: A Novel Enhanced-Domain Adaptation Mechanism for Fault Transfer Diagnosis,” IEEE Transactions on Cybernetics, vol. 53, no. 5, pp. 3128–3138, 2023.
[13] H. Fang et al., “FCDG: A Central Dogma-Inspired Approach for Cross-Domain Fault Diagnosis,” IEEE Sensors Journal, vol. 25, no. 3, pp. 3456–3465, 2025.
[14] J. N. Kahlen et al., “Improving Machine-Learning Diagnostics with Model-Based Data Augmentation Showcased for a Transformer Fault,” Energies, vol. 14, no. 20, p. 6816, 2021.
[15] Y. Wang et al., “Data Sample Augmentation for Power Transformer Fault Diagnosis
[16] via Multi-Fault Generative Adversarial Networks with Gradient Penalty Optimization,” IEEE Transactions on Power Delivery, vol. 40, no. 3, pp. 2156–2165, 2025.
[17] H. Liu et al., “Small-Sample Fault Diagnosis Method for High-Voltage Circuit Breakers via Data Augmentation and Deep Learning,” IEEE Transactions on Instrumentation and Measurement, vol. 73, p. 3537411, 2024.

Biographies

Jianfeng Yang currently serves as Director and Secretary of the General Party Branch of Ningxia Extra-High Voltage Electric Power Engineering Co., Ltd. He received his Bachelor of Engineering degree in Power System and Its Automation from Northeast Electric Power University in 1994, and his Master of Engineering degree in Electrical Engineering from North China Electric Power University in 2006. He has over 30 years of experience in power system operation, maintenance, and enterprise management. He has previously served as Deputy Chief Engineer of State Grid Ningxia Ningdong

Power Supply Company, Deputy General Manager of State Grid Ningxia Guyuan Power Supply Company, Deputy Director of the Equipment Management Department of State Grid Ningxia Electric Power Co., Ltd., and General Manager of State Grid Ningxia Integrated Energy Service Co., Ltd. Since March 2025, he has been leading Ningxia Extra-High Voltage Electric Power Engineering Co., Ltd., coordinating the large-scale deployment and practical application of the provincial-level intelligent inspection system. His current research interests include power system automation, intelligent operation and maintenance of power equipment, condition-based maintenance of equipment, and digital transformation of power grid assets.

Yuan Zhang currently serves as the Deputy Director of the Intelligent Inspection Center at Ningxia Extra-High Voltage Electric Power Engineering Co., Ltd. He received his Bachelor of Engineering degree in Electrical Engineering and Automation from Chongqing University in 2011. Within the State Grid Ningxia electric power system, he has successively held the positions of substation operation and maintenance operator, team leader, and specialist at the Intelligent Operation and Inspection Command Center. Since 2025, he has been leading the large-scale deployment and practical application of intelligent inspection systems covering the full professional scope of transmission, transformation, distribution, and direct current (DC) for the Ningxia power grid. His main research interests include autonomous UAV inspection, AI-based defect identification, multi-source data fusion, and digital transformation of power grid operation and maintenance. He has published over 20 technical papers, applied for 47 patents, and received multiple provincial and ministerial-level awards, including the First Prize of the 7th National Equipment Management and Technological Innovation Achievement.

Jiarui Yang is a Senior Engineer of Electric Power Engineering. He received his Bachelor of Engineering degree in Electrical Engineering and Automation from Xi'an University of Technology in 2008. In the same year, he joined State Grid Ningxia Electric Power Co., Ltd., and has since been engaged in the operation and maintenance management of transmission lines. His professional experience spans transmission line operation, maintenance, live-line work, emergency rescue, engineering construction, equipment retrofitting, design, and safety management. He has been granted over 20 authorized patents, including anti-falling foot pegs and detachable fall arresters. He has published the monograph Application Guide for High-Altitude Operation Equipment for Transmission and Distribution Lines (China Electric Power Press) and over 10 technical papers, including a study on inspection technology for plateau transmission corridors based on high-resolution satellite imagery data. His main research interests include intelligent operation and inspection of transmission lines, live-line working technology, and power grid safety management.

Hongyang Luo currently serves as the Project Manager of the Intelligent Inspection Center at Ningxia Extra-High Voltage Electric Power Engineering Co., Ltd. He holds a Civil Aviation Administration of China (CAAC) instructor license for vertical take-off and landing (VTOL) fixed-wing unmanned aerial vehicles (UAVs). He received his Bachelor of Engineering degree in Electrical Engineering and Automation from Shanghai University of Electric Power in 2016. He has long been dedicated to the research and application of UAV intelligent inspection technologies for extra-high voltage (EHV) and ultra-high voltage (UHV) transmission lines. He has participated in the completion of multiple key scientific and technological projects, and took part in China's first UAV rope-throwing live-line operation on the ± 1100 kV Jiquan transmission line. His current research interests include autonomous UAV inspection for transmission lines, intelligent equipment defect identification, and multi-source data fusion assessment of corridor security. He has published 2 papers in core journals, received 2 Ningxia Electric Power Science and Technology Progress Awards, and been granted 16 patents related to power UAVs.